Understanding the Epitaxial Growth of Se_xTe_y@Te Core−Shell Nanorods and the Generation of Periodic Defects

Geon Dae Moon,† Yuho Min,† Sungwook Ko, Sun-Wook Kim, Dae-Hong Ko, and Unyong Jeong*

Department of Materials Science and Engineering, Yonsei University, 134 Shiinchon-dong, Seoul, Korea. †These authors contributed equally to this work.

ARTICLE

ABSTRACT This study demonstrates solution-processed epitaxial growth of Te on Se_xTe_y nanorods and the generation of periodic defects in the core. We investigated Se_xTe_y@Te core−shell nanorods with a diameter of 40−50 nm and a length of 600−700 nm. In spite of a large lattice mismatch between the Se_xTe_y core and the Te shell, the soft character of the core and the shell at a high reaction temperature allowed epitaxial growth of Te on the Se_xTe_y nanorods. During the cooling process to room temperature (below the glass transition temperatures), the lattice mismatch between the core and the shell led to homogeneous stress along the epitaxial interface so that periodic defects were generated in the core.

KEYWORDS: epitaxial growth · defect · nanorod · core−shell structure · Se · Te

Recent advances in the synthesis of heterostructured semiconductor nanomaterials have contributed to the development of practical devices owing to their capability to control the size, composition, and band gap.[1−4] Especially, heteroepitaxial growth on a core material has been known to induce significant improvement of performance due to the carrier confinement and surface passivation.[5−7] However, the strain accumulated in the core−shell materials can constrain the growth of pseudomorphic structure by forming defects such as misfit dislocation. The study on defects in two-dimensional heteroepitaxial systems has been thoroughly conducted. A lattice mismatch larger than ∼4% (*i.e.*, 4.2% for Si/Ge and 4% for InAs/InP) has been known to induce islands or misfit dislocations except for the growth of a few atomic layers.[8] A significant difference in thermal expansion coefficients caused lattice deformation or dislocations that led to microcracks during cooling from a high growth temperature.[9] Likewise, external hydrostatic pressure can increase the residual internal stress due to mismatch in the compressibility between the film and the substrate.[10,11] Interdiffusion of ions can also result in the crystal defects.[12,13]

As compared to the generation of defects in thin films, the generation of defects in core−shell nanostructured materials has been rarely investigated. A theoretical calculation suggested that a nanowire can effectively relieve strain energy through radial relaxation, which can allow elastic strain up to 10%.[14,15] The high strain tolerance facilitated the heteroepitaxial growth between crystal planes with large lattice mismatch in core−shell structured nanomaterials: that is, Ge@Si,[16] $Si@Si_{1-x}Ge_x$,[17] GaP@GaAs[18] core−shell nanowires, and nitride nanowires on sapphire.[19] Such experimental results support the theoretical prediction on the elastic character of nanostructured materials. Ion diffusion during the chemical batch deposition formed an ordered vacancy compound (OVC) at the interface between $CuInSe_2$@CdS core−shell nanowires.[20] Very recently, Demchenko and co-workers demonstrated the formation of CdS/Ag_2S superlattice nanorods by partially exchanging Cd^{2+} by Ag^+ from CdS nanorods.[21] And they theoretically explained the mechanism by a sequential process of initial nucleation of Ag_2S at the CdS surfaces, ripening, and the formation of Ag_2S epitaxial islands in the CdS body.[22] The lattice strain field at the CdS/Ag_2S local segmental interfaces was attributed to the periodic location of Ag_2S in the superlattice nanorods.

This work reports the solution-based preparation of epitaxially grown Se_xTe_y@Te core−shell nanorods and the formation of stress-induced defects during the cooling process from a hot reaction temperature. Recently, epitaxial growth in a solution has been attracting growing attention, but the generation of defects has been rarely studied. Especially, defects caused by

*Address correspondence to ujeong@yonsei.ac.kr.

Received for review August 28, 2010 and accepted October 27, 2010.

Published online November 8, 2010.
10.1021/nn102196r

© 2010 American Chemical Society

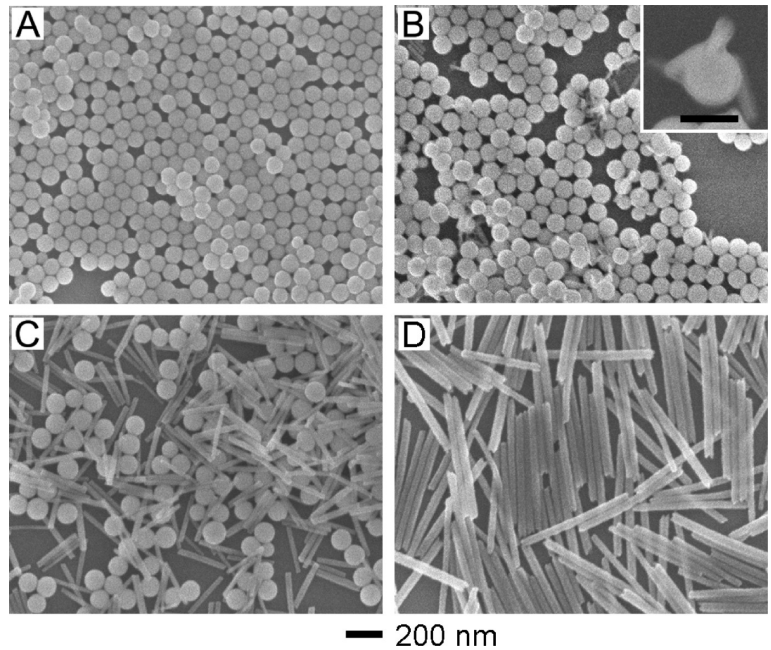

Figure 1. SEM images showing the temporal change of amorphous Se_xTe_y particles into Se_xTe_y@Te core−shell nanorods: (A) amorphous Se_xTe_y particles; (B) nucleation and growth of *t*-Se_xTe_y. Inset shows the small Se_xTe_y nanorods on the surface of a *a*-Se_xTe_y colloid. The scale bar is 100 nm; (C) further growth of *t*-Se_xTe_y nanorods through the separation from colloids; (D) Se_xTe_y@Te core−shell nanorods.

temperature variation have not been studied in solution processes. This is mainly because the reaction temperatures for the synthesis are not high enough to induce large mismatch in lattice change between the core and the shell materials after the solution is cooled to room temperature. Chalcogen core−shell structured materials can be ideal for the investigation because the glass transition temperatures (T_g) of them or their alloys should be lower than 100 °C.[23] The defects in this study were resulted by the homogeneous stress-field at the core−shell interface, not by the local stress-field at the segmental interfaces demonstrated in the previous work.[21,22]

RESULTS AND DISCUSSION

Se and Te are isomorphous semiconductors with direct bandgap. Trigonal phase with parallel arrangement of helical chains is the most stable crystalline structure.[24] Unlike the covalently bonded intrachains, the interchains are bound through the van der Waals interaction in the hexagonal order. The phase diagram calculated by Ghosh *et al.* shows that Se and Te can form a perfect solid solution.[25] They meet the four requirements mentioned in the Hume−Rothery rule[26] governing the solid solubility between metallic elements. They have identical crystal structure and the same valence electronic structure. Their atomic size difference is around 15%, which is similar to the upper limit (15%) for a complete solid solubility. And a small difference in electronegativity (0.45 in Pauling units) gives good solubility in the form of a binary solid solution. Their binary alloys (Se_xTe_y) conserve their trigonal crystalline structure.

For the experiments, we first synthesized Se_xTe_y nanorods and then epitaxially coated Te in the same batch. We used H_2SeO_3 and H_6TeO_6 as the precursors for the synthesis. The standard electrode potential of SeO_3^{2-} ($E^0 = -0.36$ V) is a little more positive than that of TeO_3^{2-} ($E^0 = -0.42$ V) in basic condition. The difference in the reduction potential leads to faster reduction of Se over Te. This difference facilitated the earlier consumption of Se atoms, resulting in Se-rich Se_xTe_y alloys. Subsequent Te reduction led to the epitaxial growth of Te on the Se_xTe_y surfaces. Owing to the identical crystal structure and intrinsic preference to 1D chain alignment along the [001] direction, a large amount of Te atoms was consumed at the both ends of the core rods, but a relatively small amount was deposited on the radial surfaces. Therefore, the core should be completely surrounded by the Te shell. The thickness of the shell can be controlled by adjusting the amount of Te precursor added in the reaction batch. Figure 1 shows the temporal change from amorphous colloids (*a*-Se_xTe_y) toward the Se_xTe_y@Te core−shell nanorods. To convince the formation of the mechanically stable Te shell, 2 equiv of Te precursor to the Se precursor was used ([H_2SeO_3]:[H_6TeO_6] = 1:2). The precursors were dissolved in hydroxylamine aqueous solution. The solution was refluxed in the presence of poly(vinyl pyrrolidone) (PVP) as a surfactant. As often observed in the synthesis of Se or Te nanowires,[27−31] the reduced atoms first formed amorphous particles, and then transformed into crystalline nanorods. The *a*-Se_xTe_y colloids through the coreduction of H_2SeO_3 and H_6TeO_6 were smooth spheres with a uniform size. Figure 1A shows

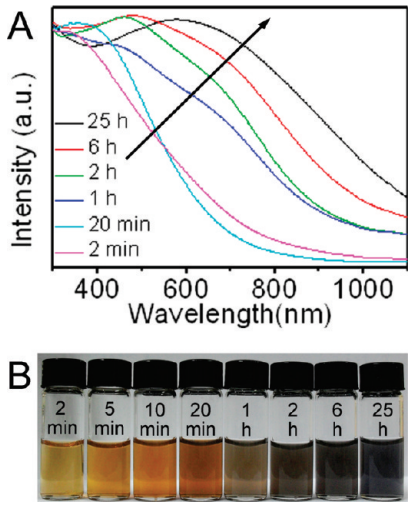

Figure 2. (A) UV−visible absorption spectra of the nanorods according to reaction time during the formation of Se_xTe_y@Te nanorods; (B) color change corresponding to the reaction time.

the alloy particles with 100 nm in diameter. The composition of the alloy particles maintained the same regardless of the reaction time. The initial small particles and the late large alloy particles had the same composition (Se:Te = 2.5:1), which indicates the reduction rate of the precursors did not change until the Se was completely consumed. The nuclei of the trigonal *t*-Se_xTe_y began to appear in 1 h on the surfaces of the *a*-Se_xTe_y colloids (Figure 1B). Once the seed of *t*-Se_xTe_y is formed, they continuously grew through the typical solid−liquid−solid (SLS) process as previously reported in the synthesis of Se or Te nanowires.[27−31] The crystallites on the surface of the particles were separated from the particles as the *a*-Se_xTe_y particles were dissolved (Figure 1C). The nanorods kept growing at the expense of *a*-Se_xTe_y until all the particles were consumed. And then, reduced Te atoms were deposited to the alloy surface for the epitaxial growth (Figure 1D). These Se_xTe_y@Te core−shell nanorods were found to be monodisperse. The average diameter was 40−50 nm, and the length was 600−700 nm.

Figure 2A displays the UV−visible absorbance change during the growth of Se_xTe_y@Te nanorods seen in Figure 1C. As the *a*-Se_xTe_y alloy particles are transformed into nanorods, the absorption in the region of 500−700 nm was enhanced. After 6 h, the peak at 600 nm started to increase. This reaction time corresponds to the beginning of the Te coating. At 24 h, the overall peak position shifted to ~600 nm due to the thick Te coating. Strong absorption at around 2.2 eV (~560 nm) was reported to come from the intermolecular electron transition between helical chains in the trigonal phase of Se.[32,33] Trigonal phase of Te also has a characteristic optical absorption at 2.21 eV from the forbidden direct transition.[32,33] Figure 2B exhibits the color change according to the reaction time.

Detailed study on the atomic composition in the core Se_xTe_y has been carried out with transmission electron microscopy (TEM) and energy dispersive spectrometry (EDS) analyses. Figure 3 shows the TEM, HR-TEM, and EDS line profiles of the Se_xTe_y nanorods obtained at an early reaction time (1 h). The dimensions of the Se_xTe_y nanorods before the shell formation were 35 nm in diameter and 370−380 nm in length. HR-TEM analysis shows well-resolved lattice fringes of the Se_xTe_y nanorods grown along the [001] direction. The interplanar spacing was 1.65 Å which is a similar value with that of trigonal Se (JSPDS 86-2244, 1.65 Å). An EDS line scan was conducted along both the radial and axial directions from the center of the nanorod. There was no conspicuous increase or decrease in the atomic ratio of Se and Te in the line scan, which indicates that Se and Te are evenly distributed in the Se_xTe_y nanorods. The overall atomic ratio from the analysis was $Se_{2.5}Te$. The inhomogeneous contrast in the TEM image (Figure 3A) is due to local variation of morphology, not by the inhomogeneous crystal structure or atomic distribution.

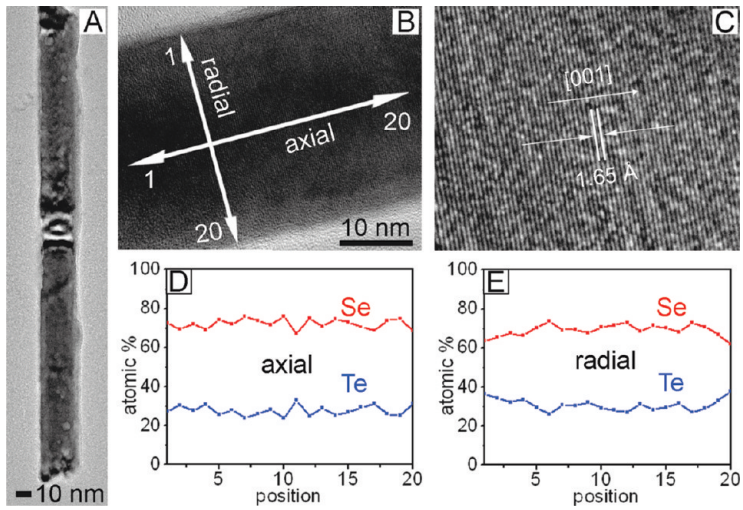

Figure 3. TEM (A, B) and HR-TEM (C) images of a Se_xTe_y nanorod synthesized at the precursor ratio ([$H_2Se_2O_3$]:[H_6TeO_6]) of 1:2. EDS line scan analyses along the axial (D) and radial direction (E) for the nanorod shown in panel B.

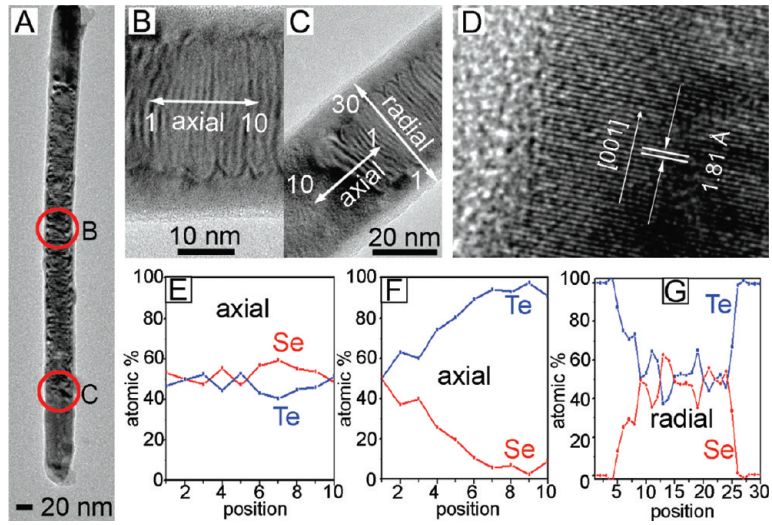

Figure 4. TEM and HR-TEM images of the Se_xTe_y@Te core−shell nanorod synthesized at the precursor ratio ([$H_2Se_2O_3$]:[H_6TeO_6]) of 1:2. Solid red circles in panel A are magnified in panels B and C. EDS line scan analysis along the axial direction in panel B is shown in panel E. Panels F and G are EDS line scans along the axial and radial direction in panel C.

Such a TEM artifact is often seen on single crystalline 1D nanostructured materials. For example, a slight bending of 1D nanomaterials in either in-plane or out-of-plane can make the electron beam to diffract in a different path, causing the contrast difference compared to the surrounding planes. To clarify the structural homogeneity of the core nanorods, we added blow-up images of the TEM and HR-TEM results to the Supporting Information (Figure S5).

The crystal structure and atomic distribution of the Se_xTe_y@Te core−shell nanorods obtained with twice the amount of Te precursor than Se precursor are exhibited in Figure 4. The spiral patterns or wrinkles in a rather regular manner inside the core region were evident (Figure 4A). The center (B) and the end (C) of the core−shell nanorods were magnified in Figure 4B,C. From the TEM images, the thickness of the Te shell in the radial direction was ∼10 nm. Figure 4 panels A and C indicate that Te atoms were actively deposited to both ends of the Se_xTe_y core rods to form thick stacking pure Te (more than 100 nm). Figure 4D exhibits the crystal planes across the boundary between the core and the shell. The image indicates that Te atoms were epitaxially deposited on the radial surface of the Se_xTe_y rods. The lattice spacing of the core−shell nanorods was ∼1.81 Å. Considering the fact that it is 1.65 Å for the $Se_{2.5}Te$ and 1.97 Å for Te (JCPDS 36-1452), the lattice spacing of Se_xTe_y@Te nanorods is ranged in the middle of $Se_{2.5}Te$ and pure Te. This lattice adjustment is considered possible owing to the reaction temperature above or near T_g of the core (53 °C) and the shell (∼90 °C).[23] Cooling down to room temperature forced the lattice of the core and the shell return to their thermodynamic size, which increased the stress at the core−shell interface. The homogeneous stress in the nanorods generated self-regulated periodic defects as observed in the form of dark stripes. Such periodic contrast was observed in any core−shell nanorod. Figure 4E shows the EDS line scan across the very middle region (B) along the axial direction. The core−shell nanorods had almost the same atomic ratio. Other EDS line-scan profiles were obtained for the tip part (C) across both the axial and the radial directions, and the atomic ratio of Te became dominant at the tip part as shown in Figure 4F. The EDS line scan across the radial direction (Figure 4G) shows that the middle part is alloyed Se_xTe_y and the edge region is a substantially Te-rich region.

Figure 5 shows blow-up TEM and HR-TEM images of the core of the Se_xTe_y@Te nanorod, visualizing the periodic arrangement of defects. It is notable that the TEM contrast was found all along the nanorods, which is different from the contrast artifact that is typically limited in a local area instead of the whole body of a specimen. We tested many core−shell nanorods and found identical periodic contrast pattern. And the contrast variation in this study was observed only in the core part of the core−shell nanorods, which is not possible in the TEM artifact. Therefore, we believe the contrast pattern in this study reflects the periodic defects. We made a plot of separation from the HR-TEM image (Figure 5C) and found the average periodicity of the defect was 2.42 ± 0.15 nm. The TEM images indicate the defects are curved toward the edges. It is well-known that a stress-induced morphological instability tends to roughen the film surface by mass diffusion in heteroepitaxial structures.[34] The strain caused by lattice mismatch drives the diffusional atomic flux along the film so that an initially flat film can evolve into an undulating profile with cusplike surface valleys. This understanding has been utilized to generate nanodots arrayed on flat surfaces.[35] Likewise, the interface of the core−shell nanorods can undergo the interfacial roughening during the cooling process, resulting in the curved defects.

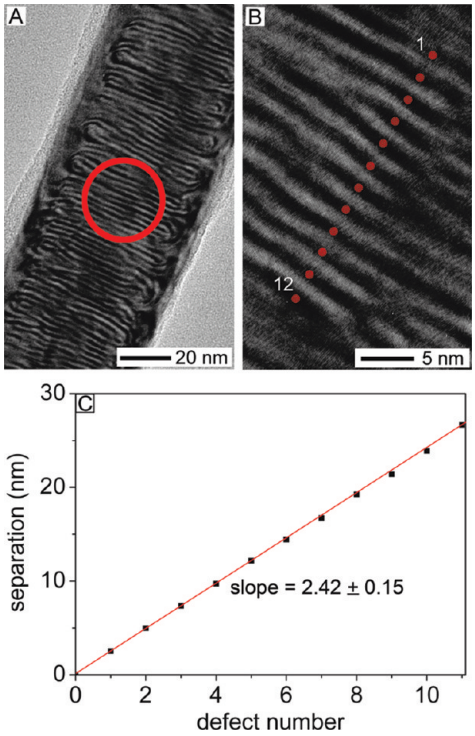

Figure 5. TEM images of the Se_xTe_y@Te core−shell nanorod showing the periodic arrangement of lateral defects in the core. A solid red circle in panel A is magnified in panel B. The periodic separation is plotted in panel C. The positions for the data are indicated in panel B.

Figure 6A is a blow-up of the defected crystal structure in the core−shell nanorod shown in Figure 4. The TEM image was taken from the middle of the nanorod. The nanorod preserved the crystalline phase indexed as the hexagonal lattice. Fourier transform analysis was conducted for the square box to clearly observe the defect orientation. The bottom images in Figure 6 are the reflections of radial (100) and axial (001) directions from the Fourier transformed image of the square box shown as an inset between Figure 6 panels B and C. While the planes along the radial direction (B) are well-aligned with no visible distortion or discontinuity, the planes along the axial direction show many blurred lines or discontinuous parts marked by red dotted circles. The strain along the radial direction is not considerable because the hexagonal stacking of the chains can be maintained even in large strain due to the isomorphous character. However, the large lattice difference of the core at room temperature (1.65 Å) from that at hot reaction batch (1.81 Å) along the axial direction during the cooling process leads to the evolution of defects in the lateral direction.

To check if the crystal structure of the core and the shell is dependent on the thickness of the shell, we conducted similar investigations with core−shell nanorods with different atomic compositions. The molar ratios ([H_2SeO_3]:[H_6TeO_6]) for additional study were varied to 2:1 and 1:1. The alloy nanorods obtained in the 1 h reaction were uniform-sized as shown in Figure 7A,E. It is noticeable that the Se_xTe_y nanorods obtained in 1 h of reaction showed the same compositional ratio regardless of the molar ratios of the initial precursors. They showed no line defects in any precursor compositions (Figure 7B,C,F,G). The HR-TEM images in Figure 7D,H indicate that the lattice distance of the Se_xTe_y nanorods was the same with that of the nanorods from 1:2 precursor ratio (Figure 3C). The EDS results displayed in Figure S1 of the Supporting Information tell that the atomic content of Se was 2.5−3 times larger than that of Te in any precursor ratios. This observation indicates that there is a limitation in the mixing ratio in the Se_xTe_y alloys. This is not consistent with the general idea that Se and Te can form complete solid solution regardless

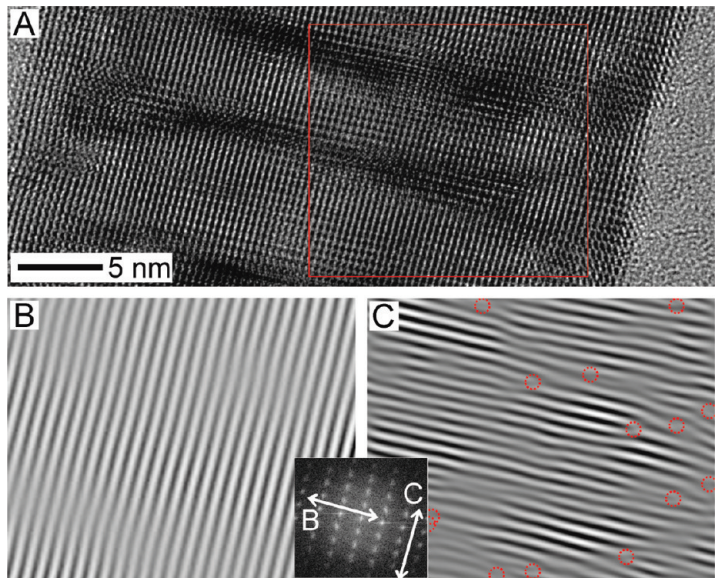

Figure 6. HR-TEM image of the Se_xTe_y@Te core−shell nanorod (A) and its fast Fourier transformed image (inset, on the bottom) obtained from the area indicated as red square. The (100) and (001) reflections from the diffraction spots in the inset show the arrangement of the lattice plane along the radial (B) and axial direction (C), respectively.

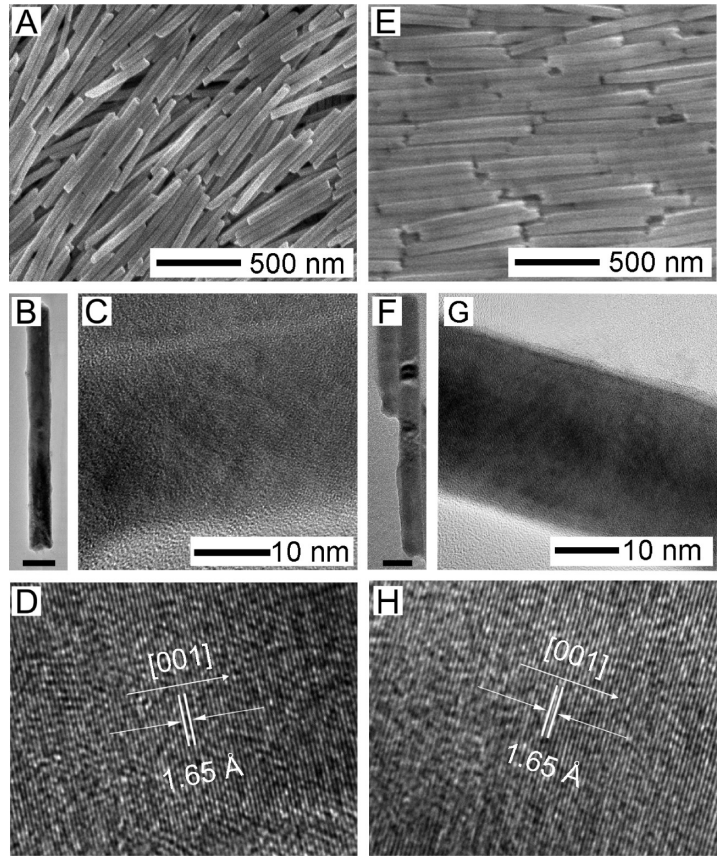

Figure 7. SEM, TEM, and HR-TEM images from the top row. The Se_xTe_y alloy nanorods synthesized at precursor ratios ([$H_2Se_2O_3$]:[H_6TeO_6]) of 1:1 (left column) and 2:1 (right column), respectively. The scale bar in panels B and F is 50 nm.

of their relative fraction. The trigonal structure of the elemental selenium and tellurium is conserved with lattice parameters slightly deviated from Vegard's law, which is an approximate empirical rule describing a linear relation between the crystal lattice parameters of an alloy and the concentrations of the constituent elements.[36] This observation might lead to a conclusion that alloyed Se and Te crystal structures exhibit substitutional disorder without any preferential short-range order. Through the experimental energy-loss spectra analysis, Katcho *et al*. inferred that Se_xTe_y alloys exhibit a high degree of substitutional disorder ruling out the

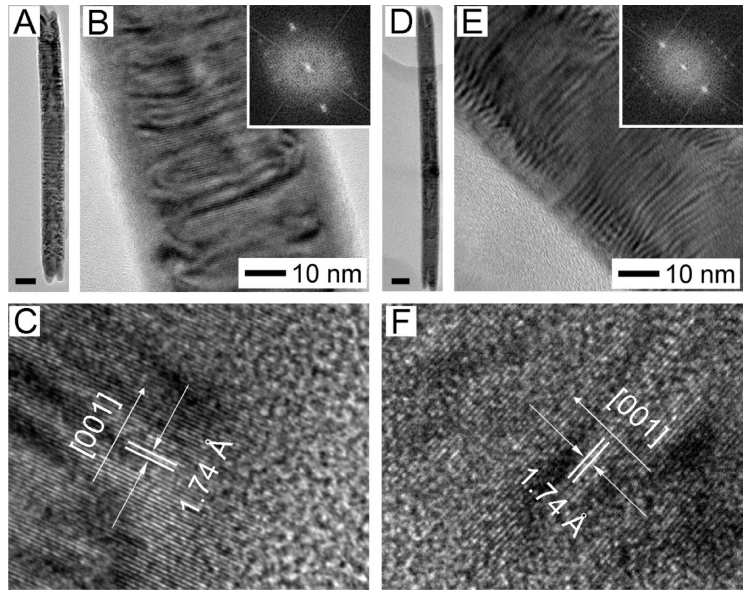

Figure 8. TEM and HR-TEM images from the top row. The Se_xTe_y@Te core−shell nanorods were synthesized at precursor ratios ([$H_2Se_2O_3$]:[H_6TeO_6]) of 1:1 (left column) and 2:1 (right column). The insets in panels B and E are Fourier transformed (FFT) images. The scale bar in panels A and D is 50 nm.

TABLE 1. Thermal Expansion Coefficients of Se and Te along *a*-Axis and *c*-Axis at Room Temperature and the Reaction Temperature[38−40]

	temp (K)	Se	Te
$\alpha_{\parallel}$ (*c*-axis)	300	-13.4×10^{-6}/K	-2.29×10^{-6}/K
	368	-14.5×10^{-6}/K	-2.47×10^{-6}/K
$\alpha_{\perp}$ (*a*-axis)	300	69.0×10^{-6}/K	29.7×10^{-6}/K
	368	80.0×10^{-6}/K	30.9×10^{-6}/K

presence of a fully ordered alternating copolymer chain of Se and Te atoms.[37] Their result and our observation indicate that perfect single crystals of Se_xTe_y have a compositional boundary. The maximum composition of Te in Se-rich alloys is considered to be ∼25% for single crystal alloys. If the atomic composition is comparable in a Se_xTe_y alloy, the material is considered to have a considerable amount of atomic disorder in their crystals. Since this report focuses on the defect generation, detailed investigation on the compositional boundary remains for a future study. The compositional limit in the core alloy assured complete consumption of Se atoms before the deposition of the pure Te for the shell.

The crystal structure of the Se_xTe_y@Te core−shell nanorods synthesized with smaller amount of Te precursors are shown in Figure 8. Their dimensions were very similar to the result in Figure 1D. The STEM images and the elemental 1D mapping (Supporting Information, Figure S2) visualize the Se_xTe_y@Te core−shell structures. From the EDS measurements (Supporting Information, Figure S3), their final core−shell nanorods were found to have the same elemental composition with the ratio of the initial precursors. It means that all the precursors were consumed to form the nanorods. Owing to the compositional limit in the core and complete consumption of the atomic sources, the thickness of the Te shell could be controlled by adjusting the ratio of Te precursor. The elemental line scans (Supporting Information, Figure S4) demonstrate that the equivalent amount of Te precursor produced 5−6 nm-thick shells and a half amount of Te precursor led to 2−4 nm-thick shells. Both ends of the nanorods were covered with thick Te crystals. In any core−shell nanorod we found similar periodic defects regardless of the atomic composition as shown in Figure 8A, B, D, E. As observed in Figure 8C,F, the same crystal lattice

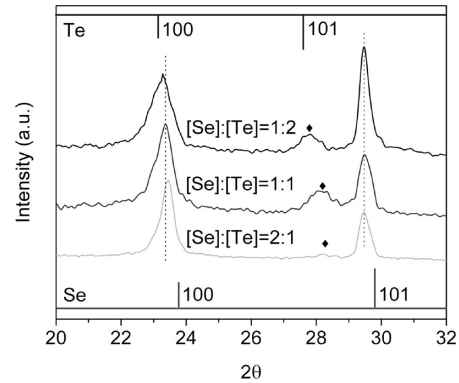

Figure 9. XRD spectra of the Se_xTe_y@Te core−shell nanorods synthesized at varying precursor ratios of Se and Te. The peaks marked by a diamond are originated from the Te shell of the Se_xTe_y@Te nanorods.

spanned across the interface between the core and the shell regardless of the atomic composition between Se and Te. The observation indicates that Te was epitaxially deposited on the core surfaces. The lattice constants of the core−shell nanorods were 1.74 Å for thin Te shells. The values are larger than those of pure Se_xTe_y nanorod counterparts seen in Figure 7. This observation again indicates that the crystals in the core and shell were adjusted to match the lattice constant between the core and the shell at the hot reaction batch. The lattice adjustment cannot be explained by a simple volume change from different thermal expansion coefficients. Table 2 exhibits the expected lattice change in the core and shell during the cooling from the hot solution simply based on the thermal expansion coefficients.[38−40] Unlike isotropic materials such as gold and silver, the anisotropic materials like Se and Te have different thermal expansion coefficients depending on the crystal directions. Se and Te have positive thermal expansion coefficients along the radial direction (*a*-axis) but a negative one along the axial direction (*c*-axis) (see Table 1).[38−40] The negative expansion along the *c*-axis is due to the polymer-like extension of the helical chains that costs lots of entropy. Thermal energy leads to entropy increase, thereby the chains shrink in the *c*-axis. Although the thermal expansion coefficient (α) drastically changes around the glass transition temperature of materials, the expected lattice changes in both the core and the shell are within 1%, which cannot explain the observed large difference in the lattice

TABLE 2. Change of Lattice Parameters Calculated from Reported Thermal Expansion Coefficients at Various Temperature. The Thermal Expansion Coefficients Cannot Explain the Lattice Change Experimentally Obtained in the $Se_{2.5}Te$@Te Core−Shell Nanorods

	Se		$Se_{2.5}Te$		Te	
	a-axis	*c*-axis	*a*-axis	*c*-axis	*a*-axis	*c*-axis
0 K (Å)	4.3712	4.9539	4.3943	5.2318	4.4522	5.9266
300 K (Å) (lattice mismatch (%))	4.4346	4.9340	4.4508 (0.9)	5.2163 (13.5)	4.4913	5.9221
368 K (Å) (lattice mismatch (%))	4.4841	4.9295	4.4878 (0.2)	5.2128 (13.5)	4.4970	5.9211
Change in lattice parameter (%) [368−300 K]	1.104	−0.0913	0.8245	−0.0671	0.1268	−0.0169

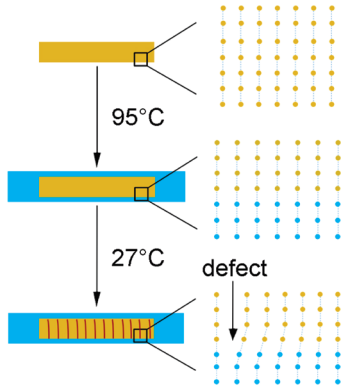

Figure 10. Schematic illustration on the evolution of periodic defects in the core of the Se_xTe_y@Te core−shell nanorod. Te atoms are epitaxially deposited on the surface of the Se_xTe_y nanorods during the synthesis at a high temperature. The Se_xTe_y@Te core−shell nanorods start to generate defects in the core in the cooling process due to the accumulated stress by lattice mismatch between the core and the shell.

constants.[23,41,42] As shown in Table 2, the Se_xTe_y core and the Te shell should experience large lattice strain along the *c*-axis for the expitaxial growth.

More quantitative change can be examined by XRD analysis. Figure 9 compares the XRD spectra from the Se_xTe_y@Te core−shell nanorods obtained with different precursor ratios. Their XRD peaks are compared with those of pure hexagonal Se and Te. The peaks of the (100) plane from the core−shell nanorods shifted to small angles as the Te compostion increased, which is consistent with the result from HR-TEM analysis. It should be noted that the peak along the [101]-direction is branched off into two peaks which can be referred to as the existence of two different phases (Se_xTe_y and Te). The left peak shows a shift with varying Se or Te molar ratio, which means that it corresponds to the Te crystalline phase in the shell part. As mentioned earlier, the Te shell thickness increased with molar ratio of Te, which can be also explained by the shift of left peaks. On the other hand, the peak on the right side along the [101] direction made no shift with varying Se and Te molar ratio, which means that homogeneous solid solutions are formed in the Se_xTe_y core region with the same atomic ratio.

Figure 10 is a proposed schematic illustration for the evolution of the periodic defects in the core of the Se_xTe_y@Te nanorods. The epitaxial interface between the Se_xTe_y core and the Te shell could be formed due to the soft nature of Se and Te at the reaction temperature in addition to the identical crystal structure of Se and Te. The Se_xTe_y single crystalline nanorods were epitaxially coated by Te in a reaction batch with a temperature (95 °C) that is higher than the glass transition temperatures of the Se_xTe_y core and Te. Even though the lattice sizes of the pure Se_xTe_y and the pure Te at room temperature are too different to preserve the epitaxial relationship, the lattices at the high temperature are considered to adjust themselves to fit the epitaxial relation. The discrepancy of the lattice parameter between Se_xTe_y and Te can bring internal strain in both phases. The strain corresponds to the tension in the core and the compression in the shell. The soft Se_xTe_y core can decrease the strain by adjusting its lattice toward that of the solid Te shell so that the lattice constant of the epitaxially grown core−shell nanorods at the hot reaction batch can be somewhere between that of the pure Se_xTe_y and pure Te. After finishing the synthesis, cooling the products to room temperature (below the glass transition temperatures) should induce a loss of their soft nature and generate a large stress field along the core−shell interface. This homogeneous stress results in the periodic defects in the relatively softer core rather than the hard Te shell.

CONCLUSION

We have synthesized epitaxially grown Se_xTe_y@Te core−shell nanorods in solution. We found that the atomic composition of the core was fixed to 2.5:1 regardless of the precursor ratio in the reaction batch. This observation indicates that there is a compositional limitation for perfect Se−Te solids. During deposition of Te atoms on the Se_xTe_y core in the hot reaction batch, the soft crystal lattices in the core and the shell adjusted themselves to meet the epitaxial relationship. Once the core−shell rods were cooled down to room temperature, the large mismatch in the thermodynamic lattice size led to a considerable stress field at the interface. The homogeneous stress field along the entire nanorods generated periodic defects confined in the relatively softer core.

EXPERIMENTAL SECTION

The chemicals used in this study were telluric acid (H_6TeO_6, ≥97.5%, Aldrich), selenious acid (H_2SeO_3, 99%, Aldrich), hydroxylamine (NH_2OH, 50 wt % in H_2O, Aldrich), poly(vinyl pyrrolidone) (PVP, M_w 55 000, Sigma-Aldrich). The deionized water was obtained using an 18-MΩ (SHRO-plus DI) system.

An aqueous solution of selenious acid (93.7−187 mg in a 25 mL of DI water) and telluric acid (111−334 mg in 25 mL of DI water) was poured in 250 mL round-bottom flask, followed by the addition of aqueous poly(vinyl pyrrolidone) solution (PVP, 1.0 g in 50 mL of DI water) under magnetic stirring at room temperature. The total amount of selenious acid and telluric acid was fixed at 1.94×10^{-3} mol with varying molar ratios of [H_2SeO_3] to [H_6TeO_6] (2:1, 1:1, and 1:2). The reaction chamber was totally sealed and set at 95 °C under a nitrogen (N_2) environment. After 1 h at 95 °C, hydroxylamine (NH_2OH) aqueous solution (2.4 mL in 20 mL of DI water) was injected in the above mixture solution with a syringe. The introduction of reducing agent made the solution color light orange in a few seconds, which indicated the formation of amorphous selenium−tellurium colloids (*a*-Se_xTe_y). The colloid suspension gradually turned brown with gray tint, indicating the nucleation of *t*-Se_xTe_y. Complete growth of Se_xTe_y@Te core−shell nanorods took 24 h and could be con-

firmed by the bluish gray color. The reaction batch was allowed to cool down to room temperature in air. The final product was collected by centrifuging (3500 rpm, 10 min) with DI water three times.

Scanning electron microscopy (SEM) images were taken by a JEOL model JSM-6700F. Transmission electron microscopy (TEM) and scanning TEM (STEM) analyses were conducted with a JEOL model JEM-2100F operated at 200 kV. Energy dispersive X-ray spectrometer (EDX) data were collected using OXFORD INCA x-sight 7421 attached to the JEM-2100F TEM. Polarized TEM images were acquired through GATAN digital microscope. XRD measurement was performed on a Rigaku II D/MAX X-ray diffractrometer at Cu Kα radiation ($\lambda = 0.1542$ nm). The UV−vis absorption spectra were analyzed by a JASCO V-500 UV/vis spectrophotometer.

Acknowledgment. This work was supported by a National Research Foundation (NRF) grant funded through the World Class University Program (R32-20031), the Pioneer Research Program (008-05103), and the Fundamental R&D Program for Core Technology of Materials by the Korean Government (MEST, MKE).

Supporting Information Available: Elemental analyses of Se_xTe_y and Se_xTe_y@Te nanorods and TEM images of them. This material is available free of charge *via* the Internet at http://pubs.acs.org.

REFERENCES AND NOTES

1. Wang, J.; Gudiksen, M. S.; Duan, X.; Cui, Y.; Lieber, C. M. Highly Polarized Photoluminescence and Photodetection from Single Indium Phosphide Nanowires. *Science* **2001**, *293*, 1455–1457.
2. Wu, Y.; Fan, R.; Yang, P. Block-by-Block Growth of Single-Crystalline Si/SiGe Superlattice Nanowires. *Nano Lett.* **2002**, *2*, 83–86.
3. Skold, N.; Karlsson, L. S.; Larsson, M. W.; Pistol, M. E.; Seifert, W.; Tragardh, J.; Samuelson, L. Growth and Optical Properties of Strained GaAs-$Ga_xIn_{1-x}P$ Core−Shell Nanowires. *Nano Lett.* **2005**, *5*, 1943–1947.
4. Smith, A. M.; Mohs, A. M.; Nie, S. Tuning the Optical and Electronic Properties of Colloidal Nanocrystals by Lattice Strain. *Nat. Natechnol.* **2009**, *4*, 56–63.
5. Lu, W.; Lieber, C. M. Nanoelectronics from the Bottom Up. *Nat. Mater.* **2007**, *6*, 841–850.
6. Lauhon, L. J.; Gudiksen, M. S.; Wang, D.; Lieber, C. M. Epitaxial Core−Shell and Core−Multishell Nanowire Heterostructures. *Nature* **2002**, *420*, 57–61.
7. Goebl, J. A.; Black, R. W.; Puthussery, J.; Giblin, J.; Kosel, T. H.; Kuno, M. Solution-Based II-VI Core/Shell Nanowire Heterostructures. *J. Am. Chem. Soc.* **2008**, *130*, 14822–14833.
8. Ertekin, E.; Greaney, P. A.; Chrzan, D. C. Equilibrium Limits of Coherency in Strained Nanowire Heterostructures. *J. Appl. Phys.* **2005**, *97*, 114325-1–114325-10.
9. Hiramatsu, K.; Detchprohm, T.; Akasaki, I. Relaxation Mechanism of Thermal Stresses in the Heterostructure of GaN Grown on Sapphire by Vapor Phase Epitaxy. *Jpn. J. Appl. Phys.* **1993**, *32*, 1528–1533.
10. Wasik, D.; Baj, M.; Siwiec-Matuszyk, J.; Gronkowski, J.; Jasinski, J.; Karczewski, G. Effect of Hydrostatic Pressure on Degradation of CdTe/CdMgTe Heterostructures Grown by Molecular Beam Epitaxy on GaAs Substrates. *J. Appl. Phys.* **2001**, *89*, 5025–5030.
11. Ritter, T. M.; Weinstein, B. A.; Kim, H. M.; Wie, C. R.; Stair, K.; Choi-Feng, C.; Funato, M. Relation Between Phase Stability and Mechanical Defects in InGa(Al)As/GaAs and ZnSe/GaAs Heterostructures under Pressure. *J. Phys. Chem. Solids* **1995**, *56*, 607–613.
12. Smigelskas, A. D.; Kirkendall, E. O. Zinc Diffusion in Allpha Brass. *Trans. AIME* **1947**, *171*, 130–142.
13. Nur, O.; Willander, M.; Hultman, L.; Radamson, H. H.; Hansson, G. V.; Sardela, M. R., Jr.; Greene, J. E. $CoSi_2/Si_{1-x}Ge_x$/Si(001) Heterostructures Formed Through Different Reaction Routes: Silicidation-Induced Strain Relaxation, Defect Formation, and Interlayer Diffusion. *J. Appl. Phys.* **1995**, *78*, 7063–7069.
14. Kavanagh, K. L. Misfit Dislocations in Nanowire Heterostructures. *Semicond. Sci. Technol.* **2010**, *25*, 024006−1−024006−7.
15. Chuang, L. C.; Moewe, M.; Chase, C.; Kobayashi, N. P.; Chang-Hasnain, C.; Crankshaw, S. Critical Diameter for III−V Nanowires Grown on Lattice-Mismatched Substrates. *Appl. Phys. Lett.* **2007**, *90*, 043115−1−043115−3.
16. Lu, W.; Xiang, J.; Timko, B. P.; Wu, Y.; Lieber, C. M. One-Dimensional Hole Gas in Germanium/Silicon Nanowire Heterostructures. *Proc. Natl. Acad. Sci.U.S.A.* **2005**, *102*, 10046–10051.
17. Clark, T. E.; Nimmatoori, P.; Lew, K.-K.; Pan, L.; Redwing, J. M.; Dickey, E. C. Diameter Dependent Growth Rate and Interfacial Abruptness in Vapor−Liquid−Solid Si/$Si_{1-x}Ge_x$ Heterostructure Nanowires. *Nano Lett.* **2008**, *8*, 1246–1252.
18. Verheijen, M. A.; Algra, R. E.; Borgstrom, M. T.; Immink, G.; Sourty, E.; Enckevort, W. J. P. van; Vlieg, E.; Bakkers, E. P. A. M. Three-Dimensional Morphology of GaP−GaAs Nanowires Revealed by Transmission Electon Microscopy Tomography. *Nano Lett* **2007**, *7*, 3051–3055.
19. Johnson, J. C.; Choi, H.-J.; Knutsen, K. P.; Schaller, R. D.; Yang, P.; Saykally, R. J. Single Gallium Nitride Nanowire Lasers. *Nat. Mater.* **2002**, *1*, 106–110.
20. Peng, H.; Xie, C.; Schoen, D. T.; Mcllwrath, K.; Zhang, X. F.; Cui, Y. Ordered Vacancy Compounds and Nanotube Formation in $CuInSe_2$−CdS Core−Shell Nanowires. *Nano Lett.* **2007**, *7*, 3734–3738.
21. Robinson, R. D.; Sadtler, B.; Demchenko, D. O.; Erdonmez, C. K.; Wang, L.-W.; Alivisatos, A. P. Spontaneous Superlattice Formation in Nanorods Through Partial Cation Exchange. *Science* **2007**, *317*, 355–358.
22. Demchenko, D. O.; Robinson, R. D.; Sadtler, B.; Erdonmez, C. K.; Alivisatos, A. P.; Wang, L.-W. Formation Mechanism and Properties of CdS−Ag_2S Nanorod Superlattices. *ACS Nano* **2008**, *2*, 627–636.
23. Abouelela, A. H.; Elmously, M. K.; Abdu, K. S. Studies of Structural Relaxation and Crystallization Kinetics of Se_xTe_{1-x} Amorphous System by DTA Measurements. *J. Mater. Sci.* **1980**, *15*, 871–874.
24. Donohue, J. *The Structure of the Elements*; John Wiley: New York, 1974; p 386−388.
25. Ghosh, G.; Sharma, R. C.; Li, D. T.; Chang, Y. A. The Se−Te (Selenium−Tellurium) System. *J. Phase Equilib.* **1994**, *15*, 213–224.
26. Mizutani, U. *Hume−Rothery Rules for Structurally Complex Alloy Phases*; CRC Press: London, 2008.
27. Song, J.-M.; Zhu, J.-H.; Yu, S.-H. Crystallization and Shape Evolution of Single Crystalline Selenium Nanorods at Liquid−Liquid Interface: From Monodisperse Amorphous Se Nanospheres toward Se Nanorods. *J. Phys. Chem. B* **2006**, *110*, 23790–23795.
28. Ma, Y.; Qi, L.; Ma, J.; Cheng, H. Micelle-Mediated Synthesis of Single-Crystalline Selenium Nanotubes. *Adv. Mater.* **2004**, *16*, 1023–1026.
29. Gates, B.; Yin, Y.; Xia, Y. A Solution-Phase Approach to the Synthesis of Uniform Nanowires of Crystalline Selenium with Lateral Dimensions in the Range of 10−30 nm. *J. Am. Chem. Soc.* **2000**, *122*, 12582–12583.
30. Mayers, B.; Xia, Y. Formation of Tellurium Nanotubes Through Concentration Depletion at the Surfaces of Seeds. *Adv. Mater.* **2002**, *14*, 279–282.
31. Gates, B.; Bayers, B.; Cattle, B.; Xia, Y. Synthesis and Characterization of Uniform Nanowires of Trigonal Selenium. *Adv. Funct. Mater.* **2002**, *12*, 219–227.
32. Joannopoulos, J. D.; Schluter, M.; Cohen, M. L. Electronic Structure of Trigonal and Amorphous Se and Te. *Phys. Rev. B* **1974**, *11*, 2186–2199.
33. Bogomolov, V. N.; Kholodkevich, S. V.; Romanov, S. G.; Agroskin, L. S. The Absorption Spectra of Single Selenium and Tellurium Chains in Dielectric Matrix Channels. *Solid State Commun.* **1983**, *47*, 181–182.
34. Yang, W. H.; Srolovitz, D. J. Cracklike Surface Instabilities in Stressed Solids. *Phys. Rev. Lett.* **1993**, *71*, 1593–1596.
35. Gao, H.; Nix, W. D. Surface Roughening of Heteroepitaxial Thin Films. *Annu. Rev. Mater. Sci.* **1999**, *29*, 173–209.

36. Grison, E. Studies on Tellurium−Selenium Alloys. *J. Chem. Phys.* **1951**, *19*, 1109–1113.
37. Katcho, N. A.; Lomba, E.; Urones-Garrote, E.; Landa-Canovas, A. R.; Otero-Diaz, L. C. Compositional Dependence of the Local Structure of Se_xTe_{1-x} Alloys: Electron Energy-Loss Spectra, Real-Space Multiple-Scattering Calculations, and First-Principles Molecular Dynamics. *Phys. Rev. B* **2006**, *73*, 214203-1–214203-8.
38. Grosse, R.; Krause, P.; Meissner, M.; Tausend, A. The Coefficients of Thermal Expansion and the Gruneisen Functions of Trigonal and Amorphous Selenium in the Temperature Range between 10 and 300 K. *J. Phys. C: Solid State Phys.* **1978**, *11*, 45–53.
39. Deshpande, V. T.; Pawar, R. R. Thermal Expansion of Hexagonal Selenium. *Curr. Sci.* **1964**, *33*, 741–742.
40. Ibach, H.; Ruin, R. Thermal Expansion of Tellurium. *Phys. Status Solidi* **1970**, *41*, 719–724.
41. Lakshmikumar, S. T.; Padaki, V. C.; Krishnapur, P. P.; Subramanyam, S. V.; Mallya, R. M.; Gopal, E. S. Ultrasonic Velocities and Thermal Expansion Coefficients of Amorphous $Se_{80}Te_{20}$ and $Se_{90}Te_{10}$ Alloys Near Glass Transitions. *J. Mater. Sci.* **1982**, *17*, 183–192.
42. Mauro, J. C.; Loucks, R. J. Selenium Glass Transition: A Model Based on the Enthalpy Landscape Approach and Nonequilibrium Statistical Mechanics. *Phys. Rev. B* **2007**, *76*, 174202−1174202−16.